7

Biomimetic Soft Robots Using IPMC

Y. Nakabo[1], T. Mukai[2], K. Asaka[3]

[1] Bio-Mimetic Control Research Center, RIKEN,
2271-130 Anagahora, Shimoshidami, Moriyama, Nagoya 463-0003, Japan and
Intelligent Systems Institute, National Institute of AIST,
1-1-1 Umezono, Tsukuba, Ibaraki 305-8568, Japan
nakabo-yoshihiro@aist.go.jp
[2] Bio-Mimetic Control Research Center, RIKEN
mukai@bmc.riken.jp
[3] Research Institute for Cell Engineering, National Institute of AIST,
1-8-31 Midorigaoka, Ikeda, Osaka 563-8577, Japan and
Bio-Mimetic Control Research Center, RIKEN
asaka-kinji@aist.go.jp

7.1 Introduction

7.1.1 Ionic Polymer-Metal Composite (IPMC)

A bimorph-type soft polymer gel actuator, which we call an artificial muscle, is an ionic polymer-metal composite (IPMC) consisting of a perfluorosulfonic acid membrane with chemically plated gold or platinum as electrodes on both sides [18, 1]. It has some excellent characteristics for robotic applications compared with other soft polymer actuators [2] as follows.

Driven with low voltage (<3 V).
Low power consumption.
Fast response (>10 Hz in water).
Mechanically and chemically durable and stable.
Soft and compliant.
Works in water (or in wet conditions).

Moreover, it has an advantage for miniaturization with its simple actuator structure. With these characteristics, we expect to apply it to micromanipulations in the bioengineering or medical fields. Our goal is to realize bioinspired soft robots, for example, a snake-like swimming robot [15, 16, 17] or a multi-degree-of-freedom (DOF) microrobot manipulator [13, 14].

The snake-like motion of a swimming robot sweeps a smaller area than a simple bending motion. It is easy to miniaturize the actuator because of its simple structure. In the future, we may be able to make robots that can swim in thin tubes or in blood vessels, or various kinds of micromanipulators in the biomedical field.

7.1.2 Multi-DOF Motion of IPMC

To realize a snake-like or a multi-DOF bending motion, we laser cut special electrode patterns on the surface of the actuator to control each segment individually.We have developed a variety of motions from this patterned actuator, including a snake-like motion. A kinematic modeling of the manipulator simply describes various multi-DOF motions of the artificial muscle. This model is applied to visual feedback control of the manipulator system using a Jacobian control method. For the feedback control, we have developed a visual sensing system using a 1 ms high-speed vision system which has a fast enough response to capture the fast actuator motion.

We have also measured the propulsion speed generated by the snake-like motion. By changing voltages and phases to each segment, we can control the direction of the propulsion. Finally, we have made the robot swim freely forward and backward by finding the optimal voltage, phase, and frequency. In this report, we show some results from simulations of the proposed manipulator control method and experimental results from visual sensing of the bending motion and snake-like swimming of the actuator.

7.2 Multi-DOF Microrobot Manipulator

7.2.1 Concept of Multi-DOF Microrobot Manipulator

Micromanipulations in bioengineering or in the medical field can be one of the applications of the artificial muscle. Our goal is to realize a multi-DOF microrobot manipulator that is automatically controlled by visual feedback, as shown in Figure 7.1.

In previous research studies on manipulators using an IPMC, Tadokoro *et al*. have fabricated a multi-DOF micromanipulator using a "3D-EFD" element [19] that consists of two arch-shaped IPMC components placed crosswise and works with a mechanism similar to that of parallel-link manipulators. Guo *et al*. have developed a multi-DOF microcatheter with active guide wires [6]. Using this catheter at a diverging point of a vessel, the direction of the catheter can be selected by the bending motion of an IPMC. However, up to this point, the kinematic modeling of multi-DOF bending motions or automatic visual feedback control have not yet been attempted. Automatic control will be required for applications of micromanipulators.

On the other hand, Mallavarapu *et al*. have implemented feedback control for dynamic bending motions in IPMC membranes [10]. They measured the bending motions of IPMC using a laser vibrometer to identify the dynamic models of bending responses to electrical stimuli and controlled them by sensor feedback. However, a laser vibrometer can only measure a distance from the sensor to a certain point of an IPMC; it cannot measure various shape changes in multi-DOF motion. For this, we need a better vision sensor.

In this research, we propose to use visual information for automatic feedback control of the IPMC. Our 1 ms vision system [12] enables high-speed and contact-

free measurement of fast shape changes in an IPMC. Also, we propose a new type of multi-DOF manipulator that is compactly designed using a patterned artificial muscle. The patterning of electrodes on an IPMC enables the multi-DOF bending motions of a manipulator with a simple structure.

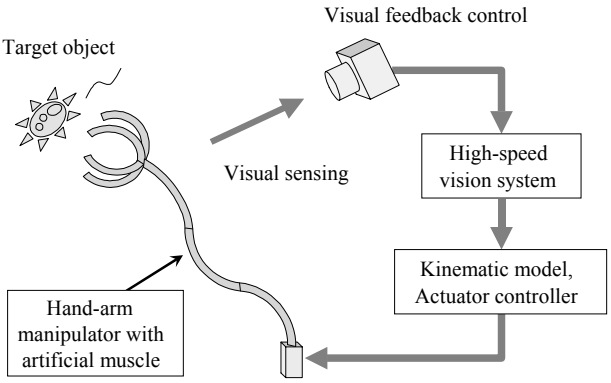

Figure 7.1. Application of multi-DOF micromanipulator with artificial muscle and visual feedback control

In the next section, we will describe details of our manipulator and how the patterning is carried out on the electrodes. The kinematic modeling for visual control is described in Section 7.4. The visual sensing system and proposal of feedback control are shown in Section 7.5. In Section 7.6, the experimental results of visual sensing are presented.

7.3 Patterned Artificial Muscle

7.3.1 Patterning with a Laser Beam

One way to realize this multi-DOF motion is to connect some of them using joints. The process of connecting them together is, however, complex, and it is difficult to make the joints flexible. So we propose another method to realize multiple degrees of freedom. In this method, we make special electrode patterns separated electrically by laser-cutting the gold-plated surface of the IPMC to control each segment individually. This method makes the IPMC bend as required without losing flexibility, and it is suitable for miniaturization because the process is simple.

The IPMC used in this study is a Nafion 117 membrane (by DuPont) five times chemically plated with gold. The thickness of the IPMC is 200 μm. After the plating, we cut a pattern on both sides of the membrane using a laser beam. By laser patterning, the thin gold layer is removed, and insulation between segments of the electrodes is achieved. By optimizing the conditions of the bursts of the laser

beam, sufficient insulation was achieved at the minimum groove size of 50 μm wide and approximately 20 μm deep.

Photomicrographs of the laser-cut pattern are shown in Figure 7.2. The left photograph shows a cross section of the membrane with a groove and a gold layer. The right one shows a closeup of the segmented electrodes seen from above the membrane. In both photographs, plated gold remained in the bright areas and was removed in dark areas. The photographs have different magnifications, but the minimum width of insulation grooves is the same (50 μm). From the photographs, the sharp lines cut by the laser can be seen.

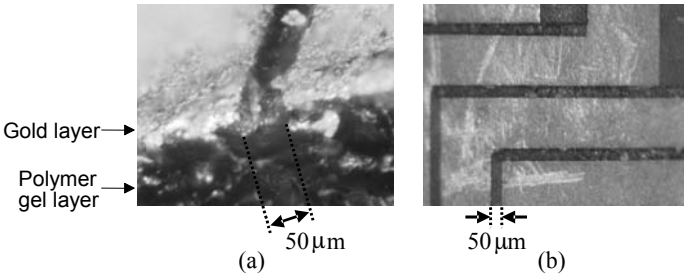

Figure 7.2. Results of laser beam patterning. (a) cross section of membrane with groove and plated gold layer, (b) patterned lines viewed from above

7.3.2 Patterning for a Multi-DOF Manipulator

Using the above laser cutting method, we have formed the electrode pattern shown in Figure 7.3. The pattern on the opposite side of the membrane has small differences only at the interconnections of electrodes.

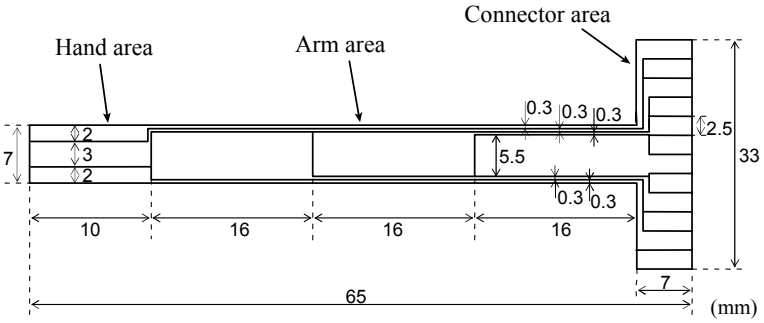

Figure 7.3. Pattern of electrodes on IPMC

The pattern on the membrane consists of three areas, a connector area, an arm area, and a hand area. The connector area is for providing electricity and mounting the manipulator to a stable base through an electric connector. The arm area is composed of three wide insulated segments for multi-DOF arm bending and many thin lines for electrical interconnections. Finally, the hand area is composed of three segments that are mechanically split so that it can grab a target object, as

shown in Figure 7.4. A photograph of the patterned IPMC is shown in Figure 7.5. Note that three beads are attached to the joints of the arm segments, which are used for visual sensing, as explained later.

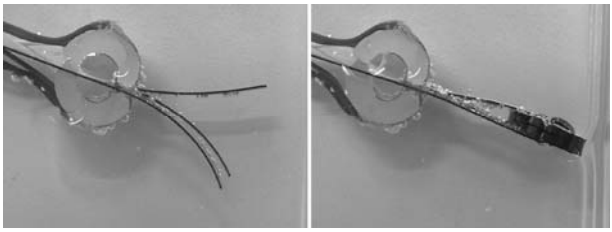

Figure 7.4. Hand with its open and grabbing position

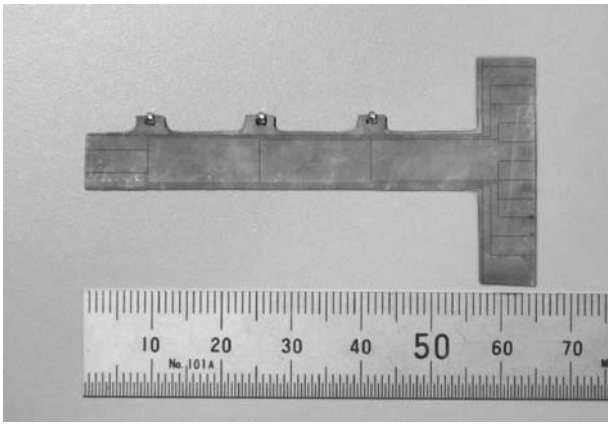

Figure 7.5. Patterned IPMC manipulator

7.4 Kinematic Modeling

7.4.1 Modeling of One-Link Kinematics

Next we propose the kinematic model of an IPMC. Our approach is similar to the modeling of conventional serial-link multi-DOF robot manipulators, but has a marked difference in that instead of joint rotation, the link itself bends on an IPMC. We treat each segment of an electrode as a link of a manipulator that can be bent independently. Figure 7.6 shows the kinematic model of a one-link bending motion. We assume that a link bends with a constant curvature. Although this assumption is not true for very large bending angles in real IPMC membranes, it is the first step in the approximation in kinematic modeling, and for small values of curvature, this is a good approximation.

Either from the kinematic model or from real IPMC bending motion, it is important to note that the position and direction of an end point of the link is restricted to one constant trajectory, that is, one link can make only one DOF motion.

7.4.2 Modeling of Multi-Link Kinematics

To realize the multi-DOF motion of a manipulator, we can connect several links in series in the same way as in conventional serial-link manipulators. In this study, as a first step in our research, we restrict the motion of the manipulator to a two-dimensional space, in which two DOF for position and one DOF for the tangential direction of the end point are controlled. We can control all three DOF independently by controlling the three links of an IPMC.

We now define coordinate systems $\Sigma_i, (i = \{0, 1, 2, 3\})$ one at the origin, one at each joint of the multi-link system, and one at the end point of an arm, as shown in Figures 7.6 and 7.7. A homogeneous transfer matrix ${}^{i}A_{i+1}$ from Σ_{i+1} to Σ_i is written as

$$ {}^{i}A_{i+1} = \begin{pmatrix} \cos(\theta_i + \alpha_i) & -\sin(\theta_i + \alpha_i) & -\dfrac{l_i}{\theta_i}(1 - \cos\theta_i) \\ \sin(\theta_i + \alpha_i) & \cos(\theta_i + \alpha_i) & \dfrac{l_i}{\theta_i}\sin\theta_i \\ 0 & 0 & 1 \end{pmatrix} \tag{7.1} $$

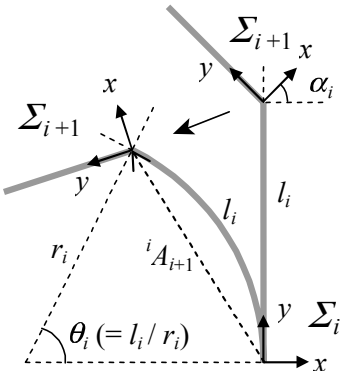

Figure 7.6. One-link kinematic modeling (note that usually $\alpha_i = 0$, as in this study)

where the certain length of a link is l_i, the curvature is $\theta_i (= r_i / l_i)$, and if the link has a certain bending angle at the joint, this angle is referred as α_i. We consider that l_i and α_i are known (also $\alpha_i = 0$ in this study).

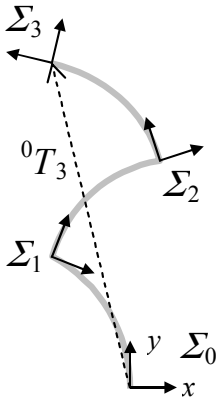

Figure 7.7. Multi-link coordinate system (note that joints are usually not bent, as in this study)

A transfer matrix from the base to the end point is calculated by multiplying each matrix of the link from the first to the last using

$$ {}^0T_3 = {}^0A_1 \, {}^1A_2 \, {}^2A_3 \tag{7.2} $$

which is shown in Figure 7.7. From this equation, we can obtain the position vector ${}^0P_e$ and rotation angle ${}^0\Theta_e$ of the end point in the base coordinate system Σ_0 as follows (where $\boldsymbol{P_e} = \left({}^0P_e, {}^0\Theta_e\right)^t = \left(P_{ex}, P_{ey}, P_{e\theta}\right)^t$) :

$$
\begin{aligned}
P_{ex} &= \frac{l_2}{\theta_2}\cos(\theta_0+\theta_1+\theta_2+\alpha_0+\alpha_1) - \frac{l_2}{\theta_2}\cos(\theta_0+\theta_1+\alpha_0+\alpha_1) \\
&\quad + \frac{l_1}{\theta_1}\cos(\theta_0+\theta_1+\alpha_0) - \frac{l_1}{\theta_1}\cos(\theta_0+\alpha_0) + \frac{l_0}{\theta_0}(\cos\theta_0 - 1) \\
P_{ey} &= \frac{l_2}{\theta_2}\sin(\theta_0+\theta_1+\theta_2+\alpha_0+\alpha_1) - \frac{l_2}{\theta_2}\sin(\theta_0+\theta_1+\alpha_0+\alpha_1) \\
&\quad + \frac{l_1}{\theta_1}\sin(\theta_0+\theta_1+\alpha_0) - \frac{l_1}{\theta_1}\sin(\theta_0+\alpha_0) + \frac{l_0}{\theta_0}\sin\theta_0 \\
P_{e\theta} &= \theta_0+\theta_1+\theta_2+\alpha_0+\alpha_1+\alpha_2
\end{aligned}
\tag{7.3}
$$

7.4.3 Position and Orientation Control Based on a Kinematic Model

To control the position and orientation of the hand of the manipulator, we have to solve an inverse kinematic problem. More specifically, we have to solve $\hat{\boldsymbol{P}}_{\boldsymbol{e}} = \boldsymbol{P_e}(\boldsymbol{\theta})$ by $\boldsymbol{\theta} = (\theta_0, \theta_1, \theta_2)^t$ from Eq. (7.3), where $\hat{\boldsymbol{P}}_{\boldsymbol{e}}$ denotes both the

objective position and orientation. However, it is quite difficult to solve Eq. (7.3); thus we use Jacobian methods for controlling and define control variables to converge to objective values. The Jacobian of $\boldsymbol{P_e}$ with $\boldsymbol{\theta}$ is defined as

$$\boldsymbol{J} = [\boldsymbol{J}_0\, \boldsymbol{J}_1\, \boldsymbol{J}_2] \tag{7.4}$$
$$\boldsymbol{J}_i = \frac{\partial}{\partial \theta_i} \boldsymbol{P_e}, \quad (i = \{0, 1, 2\})$$

Using the Jacobian, the following control, which is an inverse Jacobian method, will induce the control variable to converge to an objective value $\hat{\boldsymbol{P}}_e$ exponentially.

$$\dot{\boldsymbol{\theta}} = \lambda \boldsymbol{J}^{-1}\left(\hat{\boldsymbol{P}}_e - \boldsymbol{P_e}\right) \tag{7.5}$$

Here, λ is a given constant.

The following control, which is a transposed Jacobian method, will also induce convergence to an objective:

$$\dot{\boldsymbol{\theta}} = \lambda' \boldsymbol{J}^t\left(\hat{\boldsymbol{P}}_e - \boldsymbol{P_e}\right) \tag{7.6}$$

This is possible if an appropriate value of a constant λ' is chosen. $\boldsymbol{J}$ and $\boldsymbol{J}^{-1}$ can be calculated explicitly, but we omit such calculations because of space restrictions.

7.4.4 Simulations

We performed some simulations to verify our control methods. A block diagram of a control system simulation is shown in Figure 7.8. Results obtained by the inverse Jacobian method are shown in Figure 7.9, and those obtained by the transposed Jacobian method in Figure 7.10.

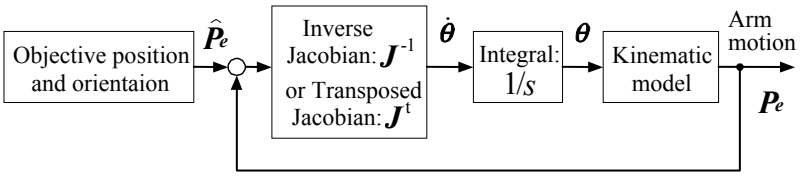

Figure 7.8. Block diagram of simulation of control system

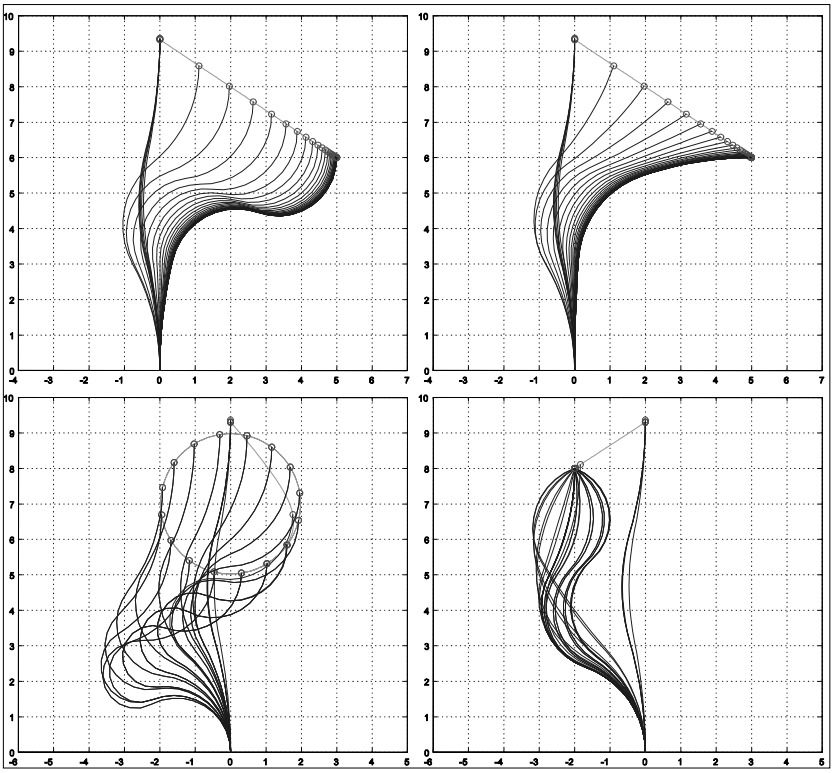

Figure 7.9. Results obtained by inverse Jacobian control (upper left: hand is kept in upper direction, upper right: its direction is changed to right, bottom left: tracking a round trajectory, bottom right: move and swing)

All results show that each segment of an IPMC membrane is properly bent to realize the given trajectories of positions and orientations of the end points. By the inverse Jacobian method, trajectories in Cartesian coordinates are straightforward and exponentially converged to the objective, where they are not by the transposed Jacobian. However, an inverse Jacobian is not stable near a singular position, in this case, at the upright position, whereas a transposed Jacobian is defined and stable at any point. From these results, it is confirmed that we can control all three DOF of a 2-D manipulator by the proposed methods.

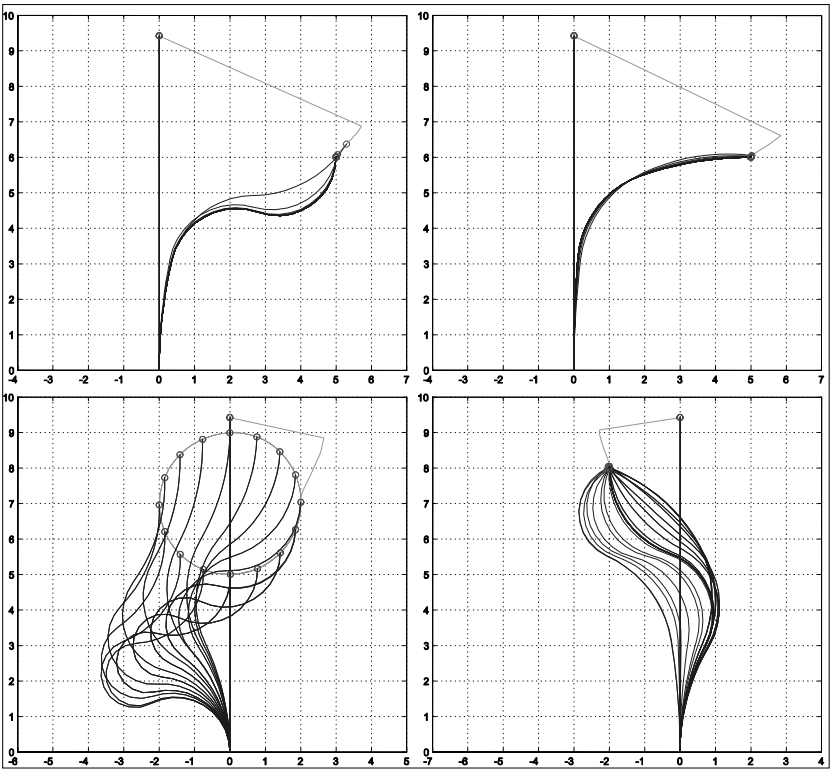

Figure 7.10. Results obtained by transposed Jacobian control (upper left: hand is kept in upper direction, upper right: its direction is changed to right, bottom left: tracking a round trajectory, bottom right: move and swing)

7.5 Visual Sensing and Control System of a Multi-DOF Manipulator

7.5.1 Visual Sensing System

To realize the proposed control method, we need to determine the error of the end point $\boldsymbol{P_e}$ from an objective and the curvature $\boldsymbol{\theta}$ to calculate the Jacobian $\boldsymbol{J} = \boldsymbol{J}(\boldsymbol{\theta})$ in real time.

Because the artificial muscle is a soft actuator and the membrane itself bends, limited types of sensor can be used. We propose the use of a vision sensor that can measure the overall shape changes of multi-DOF motions by contact-free sensing. However, conventional CCD cameras do not have sufficient sampling speed due to their limited video transfer rate. Thus, we used a 1 ms high-speed CPV system [12], which can capture an image and execute a processing algorithm in a cycle time of 1 ms.

Light colored beads on each joint of the manipulator are used as references for the coordinate systems. The curvatures of the links are calculated using (see Figure 7.6)

$$\theta_i = 2\arctan\left(-\frac{{}^{i}P_{i+1x}}{{}^{i}P_{i+1y}}\right), \quad (i = \{0, 1, 2\}) \tag{7.7}$$

where ${}^{i}\boldsymbol{P}_{i+1} = \left({}^{i}P_{i+1x}, {}^{i}P_{i+1y}\right)^{t}$ is the position vector from the origin of Σ_i to Σ_{i+1} in the coordinate system of Σ_i.

7.5.2 Control System

The proposed feedback control system is shown in Figure 7.11. It includes a visual sensing system, a Jacobian and error estimation component, a control component, and a multi-DOF patterned artificial muscle (IPMC). Figure 7.12 shows the camera head of our visual sensing system and an IPMC manipulator. The manipulator is hung in water above the electric connector.

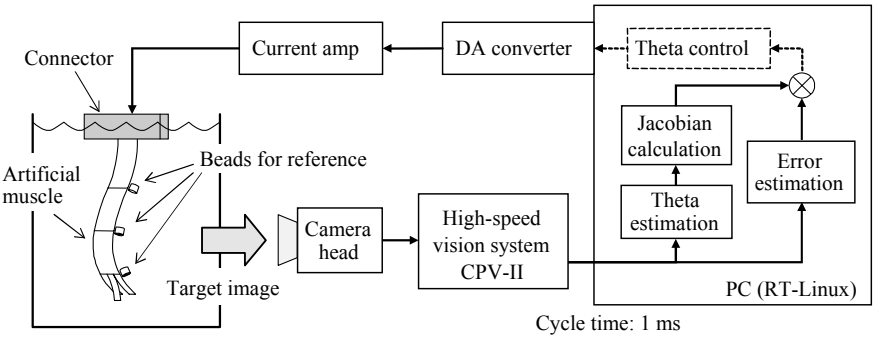

Figure 7.11. Block diagram of visual sensing and control system

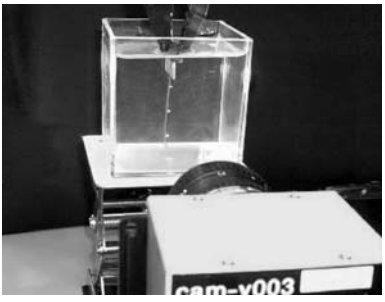

Figure 7.12. Camera head of vision system and artificial muscle

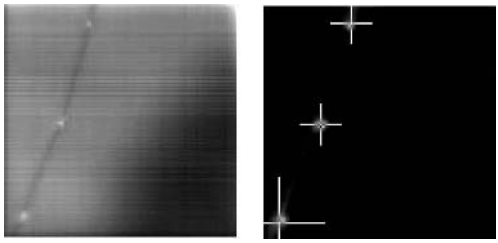

Figure 7.13. Image obtained by vision system (left), and result image of recognition of reference beads (right)

7.6 Experimental Results of Multi-DOF Manipulator

In this study, we have realized all parts of the control system shown in Figure 7.11 except the theta control stage which is enclosed by the dotted line in the figure.

First, we tested the multi-DOF bending motion of the IPMC. A problem encountered was the voltage drop through interconnection lines on the IPMC. We found that more than 3V is needed at the connector area to provide sufficient voltage at each link segment (up to 2V). With such a high voltage, the electrolysis of water occurs and this heat causes breakdown of the thin interconnections. In subsequent experiments, we wired electrodes directly to each arm segment.

Next, we conducted experiments using the visual sensing system. We applied sine waves with maximum voltages of 2V and cycle times of 1s to the arm segments. First, their phases are synchronized so that a swing motion of the arm was made. An image obtained using the high-speed vision system and a result of recognition of the reference beads are shown in Figure 7.13. The center points of three reference beads are identified accurately, as shown by three crosses.

The curvatures estimated from the images by online calculation using Eq. (7.7) are shown in Figure 7.14. The reconstructed bending motion of the IPMC using the curvature data and the proposed kinematic model is shown in Figure 7.15.

In the next experiment, we applied the same sine waves with a cycle time of 1.5s; their phases are shifted 60° from each successive segment.

A snakelike motion has been realized by a phase-shifted sinusoidal input. Online estimated curvatures of a bending motion caused by the shifted sine waves with a cycle time of 1.5s are shown in Figure 7.16. The bending motions reconstructed from the curvature data and kinematic model are shown in Figure 7.17. The sequential photographs of a real bending motion caused by the shifted sine waves with a cycle time of 3s are shown in Figure 7.18.

From the experimental results of both estimation and reconstruction, we can see that the estimated parameters match the real motions of the segmented IPMC. Our vision system and algorithms work properly for sensing a multi-DOF IPMC manipulator.

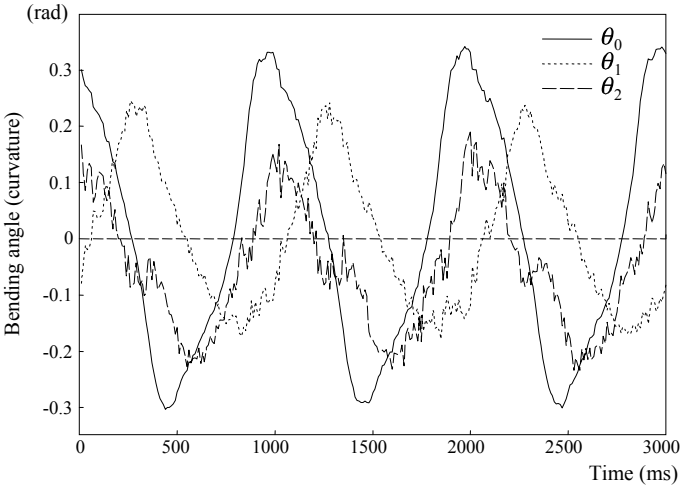

Figure 7.14. Results of estimation of curvature in a swing motion

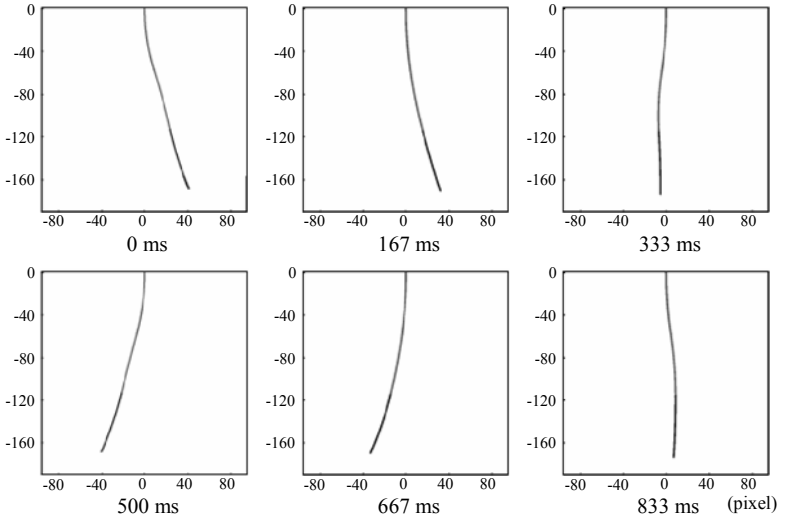

Figure 7.15. Link motions reconstructed by curvature data and the kinematic model in a swing motion (from left to right and top to bottom)

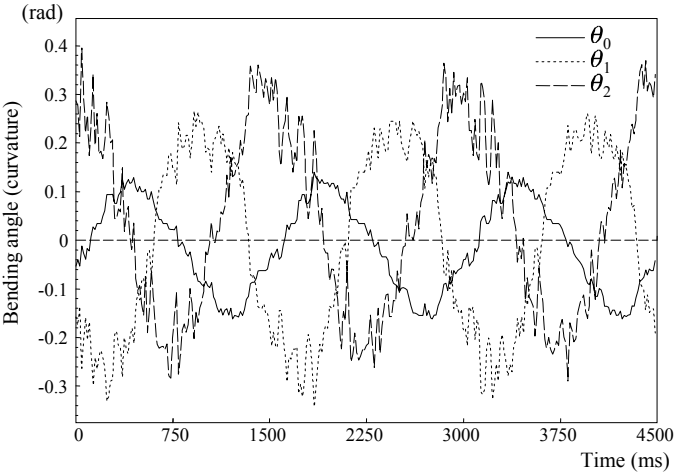

Figure 7.16. Results of estimating curvature in a snake-like motion

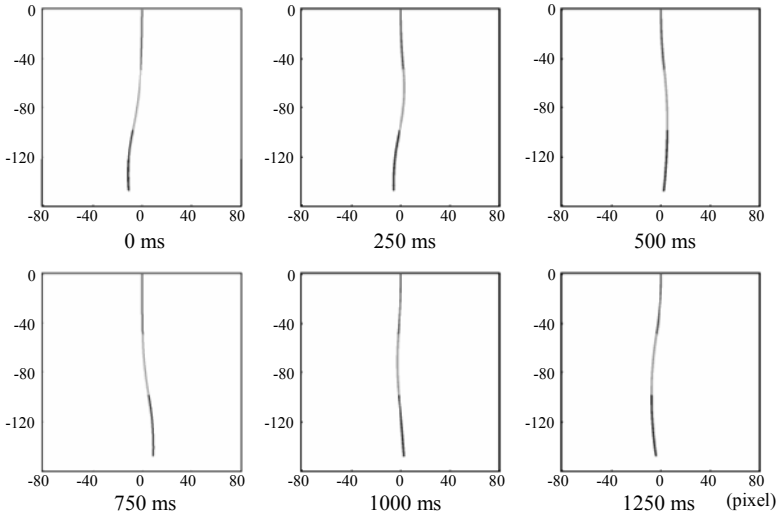

Figure 7.17. Link motions reconstructed by curvature data and the kinematic model in a snake-like motion (from left to right and top to bottom)

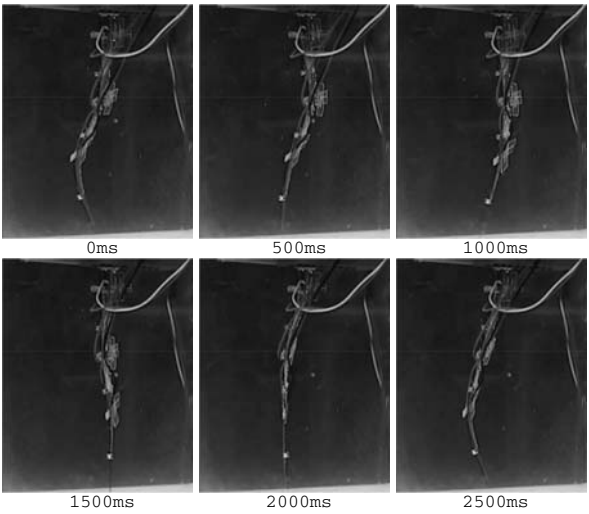

Figure 7.18. Snakelike bending motions caused by phase-shifted sine waves

7.7 Snake-Like Swimming Robot

7.7.1 Concept of a Snake-Like Swimming Robot Using IPMC

The underwater microrobot is also a novel and potential application of the IPMC. There are several studies on underwater propulsion robots using the IPMC. For example, Mojarrad and Shahinpoor developed a propulsion robot using the IPMC as a fin to generate a forward impelling force [11]. Guo *et al*. developed a fish-like microrobot that uses two actuators for right and left turning [5]. However, in these studies, a strip-shaped IPMC is used, which generates only a simple bending motion, thus a backward movement could not be achieved, although forward propulsion and a directional change have been realized. Not only that, such a simple bending motion has a lower efficiency than a snake-like wavy motion in propulsion, which has been found by the biological analysis of the swimming mechanism of fish or other living creatures. To realize more complex motions, such as multi-DOF motions, a patterned IPMC, each segment of which could be bent individually, is required.

Now, we are aiming at realizing a swimming robot with a patterned IPMC that bends like a snake. A snake-like motion sweeps a smaller area than a simple bending motion. Thus, it is suitable for future swimming robots in thin tubes, such as blood vessels, as shown in Figure 7.19. We input voltages as phase-shifted sinusoidal waves to each segment of the patterned IPMC, so that a progressive wave is generated as its bending motion. The system can control its impelling force and swimming directions left, right, forward, and backward. We can change amplitudes, frequencies, and phases of input waves to control the speed and

direction of the robot propulsion. In this study, we describe the patterned IPMC and its propulsion by experiments.

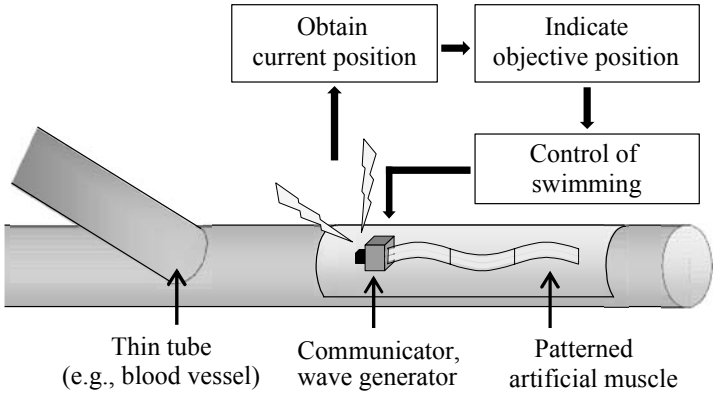

Figure 7.19. Concept of a snake-like swimming robot

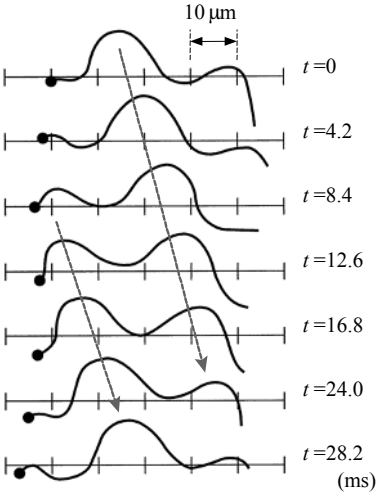

Figure 7.20. Swimming of sperm of starfish [7]

7.7.2 Natural Creatures Swimming in Water

There are many creatures swimming in water, among which eels, morays, and sea serpents can control their swimming directions forward and backward. Their bodies, called anguilliform, are slender or long and thin like a ribbon. The heights of their bodies are almost constant from head to tail. When they move forward, they generate a forward impelling force by sending progressive waves toward the rear along their bodies [20, 3]. Similarly, to move backward, they send progressive waves toward the front along their bodies. As an example of swimming by

progressive waves, the swimming of the sperm of starfish is shown in Figure 7.20 [7].

The snake-like swimming of the anguilliform is most efficient in a high-Reynolds-number environment such as that on a microscale. It is also efficient for slender body fishes in a normal-scale underwater environment, including carps and gibels. A wavy motion is better at reducing an angular recoil from water than a simple bending motion [8].

7.8 Patterning of IPMC for a Swimming Robot

7.8.1 Comparing Single- and Multi-DOF Motions

Although many natural creatures use a wavy or snake-like motion, on the other hand, a single artificial muscle in the form of an IPMC cannot generate various motions on its own. The static form of an IPMC depends uniquely on an input voltage, indicating that it has only a single DOF. Figures 7.21 (a) and (b) show simulations of a simple swing motion of an IPMC and a multi-DOF motion of the IPMC controlling its three segments independently. These simulations are based on the kinematic model in which a constant curvature for each segment of the IPMC is assumed [14]. A sinusoidal input is given to the IPMC in (a) and 60° phase-shifted sinusoidal waves are given to each segment in (b). A wavy motion is realized in (b).

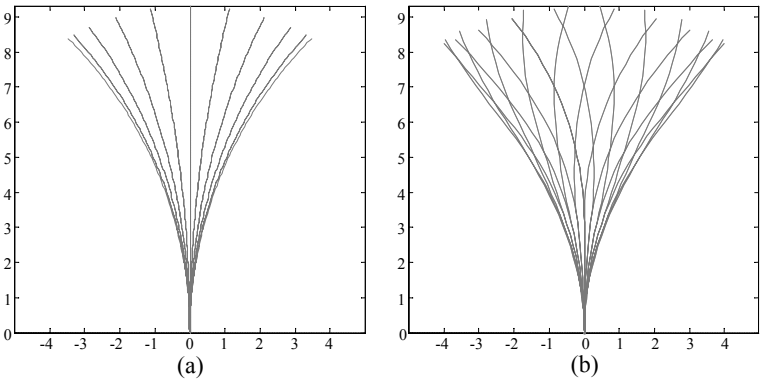

Figure 7.21. Simulations of bending motion: (a) 1-DOF simple bend and (b) 3-DOF snake-like bend

7.8.2 Patterning of IPMC for Snake-Like Swimming

In our previous study, we have developed a laser patterning method that enables electric insulation at a minimum gap width of 50 μm. However, in this study, to create a simple pattern such as that shown in Figure 7.22, a tentative method,

which is the carving of the IPMC surfaces with a small hand chisel, is sufficient. We verified the electric insulation between segments.

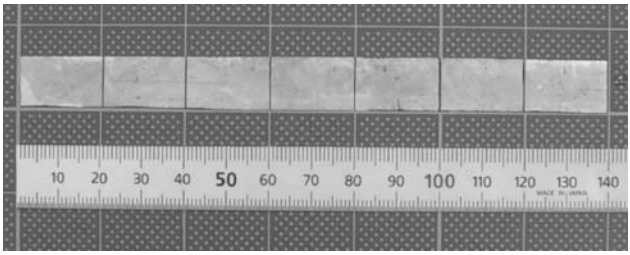

Figure 7.22. Patterned artificial muscle

The IPMC used in this study was a Nafion 117 membrane (by DuPont) five times chemically plated with gold. The thickness of this IPMC was 200 μm. This IPMC was electrically isolated to seven segments. To input voltages, we used seven connectors and electric wires touching each segment directly. They were small and sufficiently thin not to disturb the movement of this IPMC. We also used floats to prevent this IPMC from sinking (Figure 7.23).

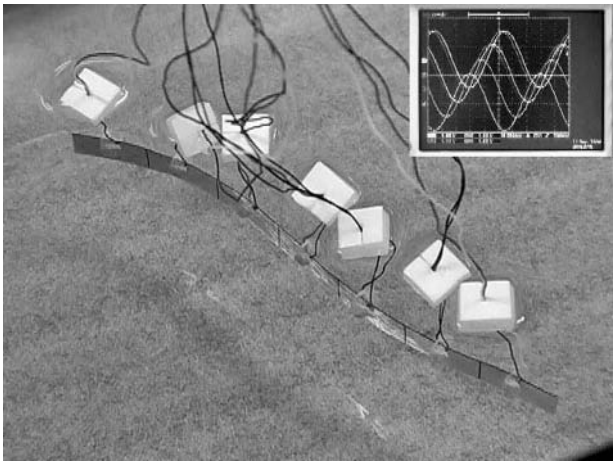

Figure 7.23. Snake-like swimming robot with patterned artificial muscle

7.9 Control System of Snake-Like Swimming Robot

A block diagram of the control system of the swimming robot is shown in Figure 7.24. Input waves are calculated by a PC and converted to voltage signals by a DA converter. Then, currents of signals are amplified and sent to corresponding segments of the IPMC. Control signals for latter experiments are composed of

sinusoidal waves, whose amplitudes AV and frequencies f Hz are constant, but their phases are delayed (0, θ, 2θ,...)deg from segment 1 to segment 7, as shown in Figure 7.25.

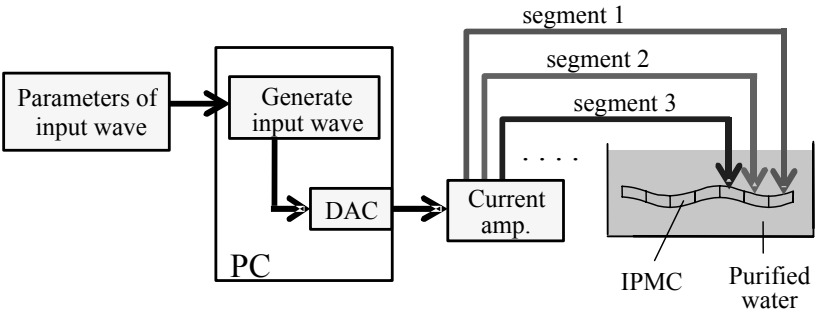

Figure 7.24. Block diagram of snake-like swimming robot

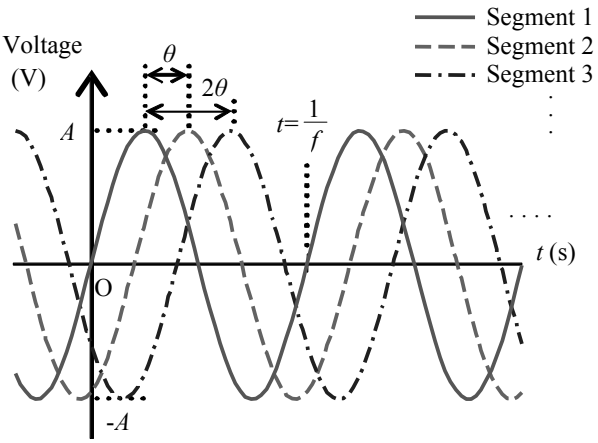

Figure 7.25. Input wave of snake-like bending motion

7.10 Experiments of Snake-Like Swimming Robot

7.10.1 Forward and Backward Propulsions

We first investigated the forward and backward propulsions by the snake-like bending motion of the patterned IPMC. An experimental system for measuring speed is shown in Figure 7.26. A long string and a long balancing rod cancel the obstruction of electric wires and allow free movement of the floats in forward and backward directions.

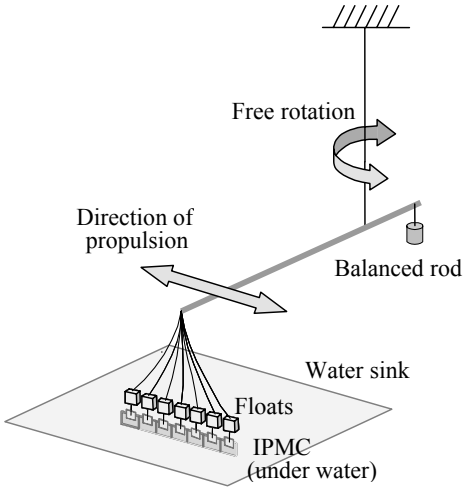

Figure 7.26. Experimental setup for measuring propelling speed

We searched for an optimal condition for propulsion by changing the frequency f and phase shift θ. In our experiments, an amplitude of input waves is fixed at $A = 2\,\mathrm{V}$. Although a high voltage generates a large bending motion and a large impelling force, a voltage of more than 2V induces the electrolysis of water and this heat harms the IPMC.

Figure 7.27 shows the change in propelling speed with input frequency f, where error bars show standard deviations of the trials. Sine waves with the amplitude $A = 2\,\mathrm{V}$ and phase delay $\theta = 60°$ are input to each segment of the patterned IPMC from frequencies $f = 1$ to 10Hz. Speeds were calculated by measuring the forward or backward distance traveled in 10s. We obtained the maximum speed at the frequency f of 2Hz.

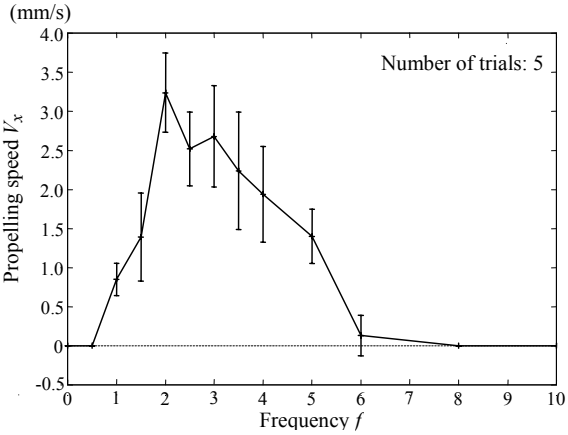

Figure 7.27. Propelling speed vs. frequency

We also investigated the change in propelling speed with phase shift. The phase delays are $\theta = -180°$ to 180°, and the amplitude A = 2V and frequency f = 2Hz with which our IPMC produced the maximum speed in the first experiment.

Figure 7.28 shows the results of this experiment, where error bars show standard deviations of the trials. We successfully controlled the propelling direction of the IPMC forward or backward by changing the direction and speed of propagation of waves along the body by advancing and delaying the phases of the sine waves. We obtained the maximum speed at the phase shift θ of ±60°. Figure 7.29 shows the input voltage and current response of the IPMC. Figure 7.30 shows the bending motions of forward and backward propulsions.

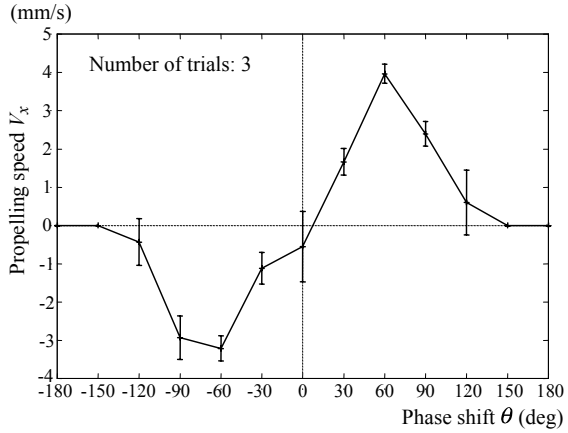

Figure 7.28. Propelling speed vs. phase shift

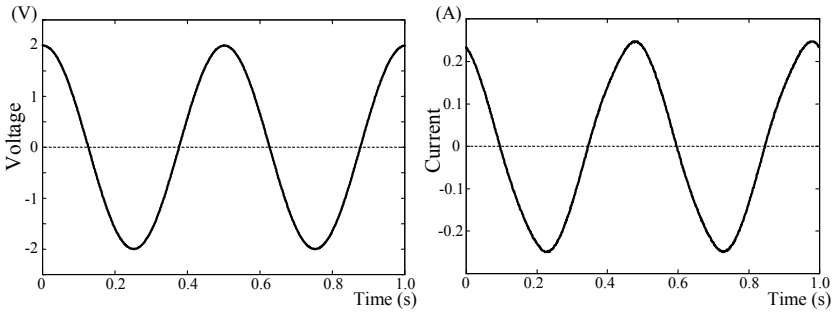

(a) Input voltage (b) Current response

Figure 7.29. Input voltage and current response of forward propulsion

7.10.2 Right Turn and Left Turn

We next attempted the right turn and left turn of the patterned IPMC. In generating right and left directed biased forces for turning the robot, simply biased sine waves are not effective because nonlinear dynamics of bending responses of an IPMC cancels averagely biased input voltages in a few seconds. Instead of using the biased sine waves, we propose the use of a sawtooth-like waveform, whose rising and falling times of input voltage are not uniform, as shown in Figure 31. In this case, the frequencies during the rising and falling of the input waves are different. The first experiment suggests that the change in frequency induces the change in impelling force; thus, the direction of propulsion may be biased to the right or left by the proposed sawtooth-like waveform.

An experimental setup for measuring turning speed is shown in Figure 7.32. A long string allows free rotation of the robot in the right and left directions.

To evaluate the proposed sawtooth-like waveform, we conducted an experiment to investigate the turning speed of the IPMC by changing the ratio of the rising time to the falling time of the input waves (T_1/T_2) from 0.026 to 38.8 using a piecewise sinusoidal waveform, as shown in Figure 31. The amplitude, phase delay, and total frequency of the oscillating waves are fixed at A = 2V, θ = 60° and f = 2Hz with which the IPMC produced the maximum speed in the previous two experiments. The turning speeds are calculated by measuring the angle of turning right or left in 10s.

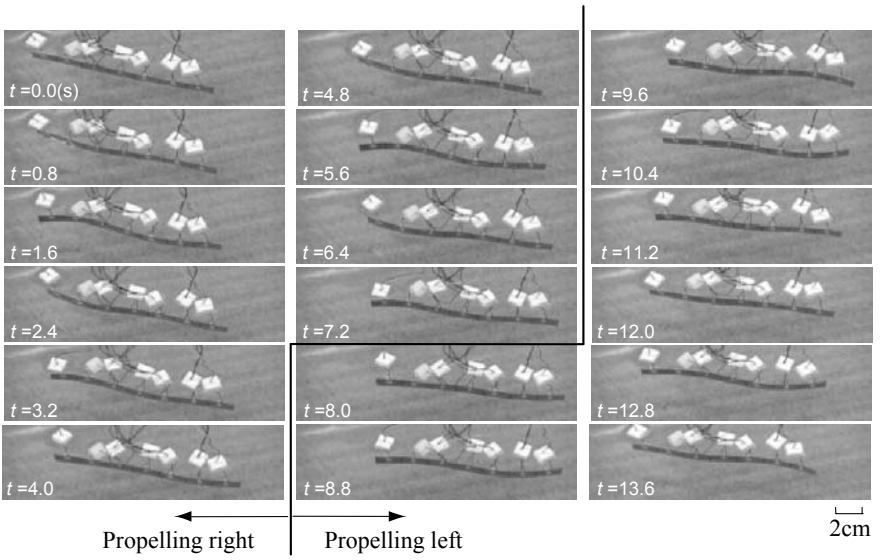

Figure 7.30. Forward and backward propulsions

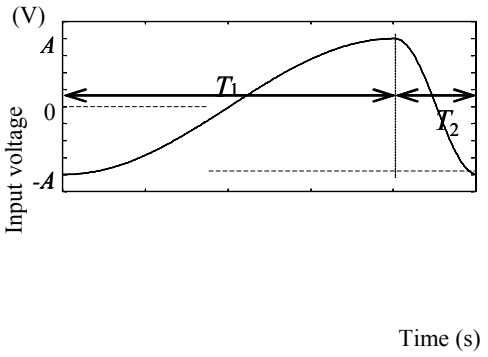

Figure 7.31. Sawtooth-like input waveform for turning

The results are shown in Figure 7.35, where error bars show standard deviations of the trials. From these results, we found that the robot can be turned right and left by changing the ratio of the rising time to the falling time of the proposed piecewise sinusoidal waveform. Figures 7.33 and 7.34 show the input voltages and current responses of the IPMC that induce the maximum left-turn and right-turn speeds of the robot. Figure 7.36 shows the bending motion of the IPMC for the right turn and left turn.

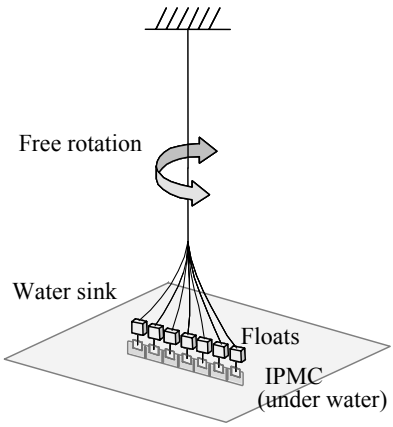

Figure 7.32. Experimental setup for measuring turning speed

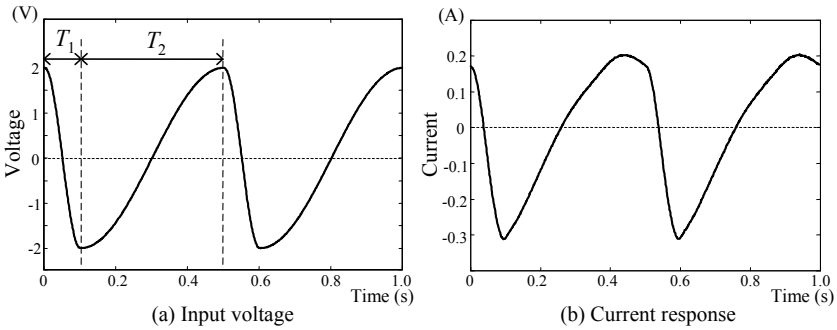

Figure 7.33. Input voltage and current response of left turn

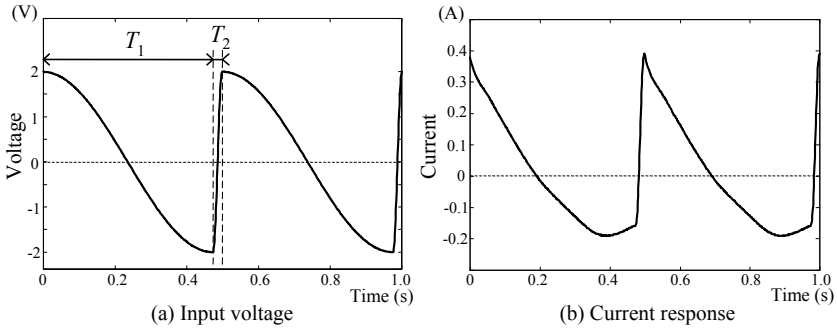

Figure 7.34. Input voltage and current response of right turn

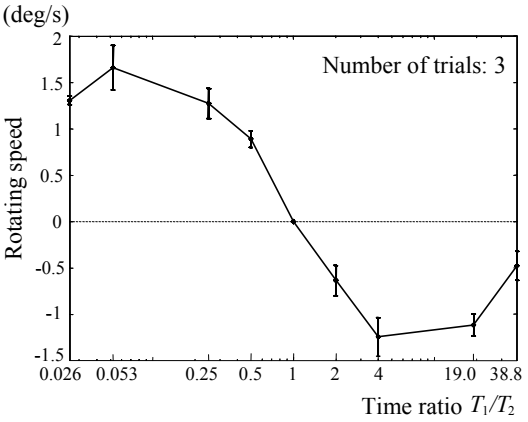

Figure 7.35. Rotating speed vs. time ratio

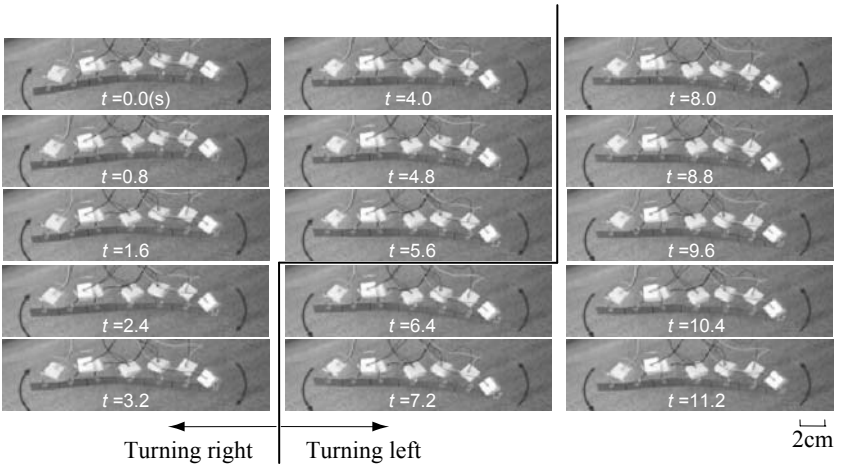

Figure 7.36. Right turn and left turn

7.11 Modeling of Propulsion and Turning

In this section, we present a propulsion model of the snake-like swimming motion to explain the experimental results of the propulsion and turning of the IPMC. We first consider the forward and backward propulsions and then the right turn and left turn based on a propulsion model for microorganisms [4] that swim with a snake-like motion.

7.11.1 Modeling of Forward and Backward Propulsions

We first estimate the propulsion force generated by the bending motion of the IPMC. The x axis is aligned along the opposite direction of the forward

propulsion of the IPMC, and the z axis indicates the amplitude of the bending motion.

As shown in Figure 7.37, when a small part of an IPMC δs moves along the z direction with its speed of V_z, δs receives a drag force δL_z whose direction is tangent to δs, and a resistance force δN_z whose direction is normal to δs from a fluid (in this case, water). If $|\delta s| << 1$ and $V_z << 1$, we can assume that the drag and normal resistance forces are proportional to speeds relative to each direction. They can be calculated by

$$\delta L_z = C_L V_z \sin\theta \, \delta s$$
$$\delta N_z = C_N V_z \cos\theta \, \delta s$$

where C_L and C_N are the drag and normal resistance coefficients and θ is the tangent angle of δs.

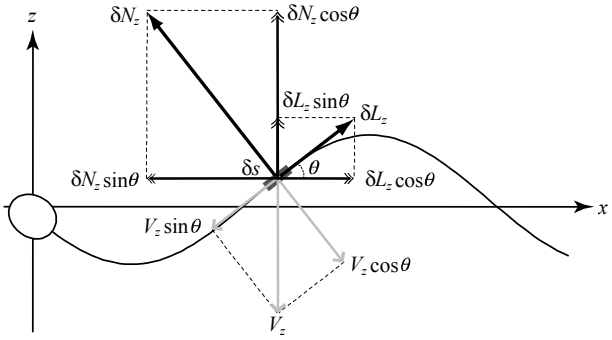

Figure 7.37. Force generated by bending along the *z* axis

Similarly, the forces induced by the x directed motion V_x of δs can be calculated by

$$\delta L_x = C_L V_x \cos\theta \, \delta s$$
$$\delta N_x = C_N V_x \sin\theta \, \delta s$$

as shown in Figure 7.38.

Thus, the total drag force δL and resistance force δN induced by V_x and V_z are calculated by

$$\begin{aligned} \delta L &= \delta L_z + \delta L_x \\ &= C_L \left(V_z \sin\theta + V_x \cos\theta \right) \delta s \end{aligned} \tag{7.8}$$

$$\begin{aligned}\delta N &= \delta N_z + \delta N_x \\ &= C_N\left(V_z \cos\theta - V_x \sin\theta\right)\delta s\end{aligned} \tag{7.9}$$

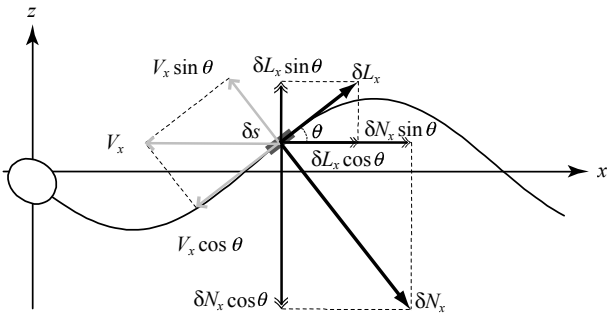

Figure 7.38. Force generated by bending along the x axis

The x directed force δF_x applied by the fluid can be calculated by summarizing each x element of δL and δN as

$$\begin{aligned}\delta F_x &= \delta N \sin\theta - \delta L \cos\theta \\ &= \left[\left(C_N - C_L\right)V_z \sin\theta\cos\theta - V_x\left(C_N \sin^2\theta + C_L \cos^2\theta\right)\right]\delta s \\ &= \frac{\left(C_N - C_L\right)V_z \tan\theta - V_x\left(C_L + C_N \tan^2\theta\right)}{1+\tan^2\theta}\delta s\end{aligned} \tag{7.10}$$

From this equation, we can see that the direction of propulsion is forward when $C_N > C_L$ at $V_x = 0$.

Now, let $z = z(x,t)$ be the position of the IPMC along the x axis thus, $V_z = dz/dt$ and tan $\theta = dz/dx$. Equation (7.10) can be rewritten as

$$\frac{dF_x}{ds} = \left\{\left(C_N - C_L\right)\frac{dz}{dt}\frac{dz}{dx} - V_x\left[C_L + C_N\left(\frac{dz}{dx}\right)^2\right]\right\}\Bigg/\left[1+\left(\frac{dz}{dx}\right)^2\right] \tag{7.11}$$

When $\theta << 1$, $(dz/dx)^2 \cong 0$ and $ds \cong dx$; thus, (7.11) can be rewritten simply as

$$dF_x = \left[\left(C_N - C_L\right)\frac{dz}{dt}\frac{dz}{dx} - C_L\overline{V}_x\right]dx \tag{7.12}$$

where $\overline{V}_x$ is the average speed of the IPMC propulsion.

Finally, the total propelling force F_x of the IPMC is calculated by

$$F_x = \int_{x=0}^{x=l} dF_x \tag{7.13}$$

where l is the length of the IPMC.

7.11.2 Modeling of Right Turn and Left Turn

We now determine the moment of force generated by the bending motion of the IPMC. From Eqs. (7.8) and (7.9), the z directed force δF_z applied to δs by the fluid is calculated by summarizing each z element of δL and δN as

$$\begin{aligned}\delta F_z &= \delta N \cos\theta - \delta L \sin\theta \\ &= \left[V_z\left(C_N \cos^2\theta + C_L \sin^2\theta\right) - \left(C_N - C_L\right)V_x \sin\theta\cos\theta\right]\delta s \\ &= \frac{V_z\left(C_N + C_L \tan^2\theta\right) - \left(C_N - C_L\right)V_x \tan\theta}{1+\tan^2\theta}\delta s\end{aligned} \tag{7.14}$$

By substituting $V_z = dz/dt$ and $\tan\theta = dz/dx$ to (7.14), the following equation is obtained.

$$\frac{dF_z}{ds} = \left\{\frac{dz}{dt}\left[C_N + C_L\left(\frac{dz}{dx}\right)^2\right] - V_x\left(C_N - C_L\right)\frac{dz}{dx}\right\} \Bigg/ \left[1+\left(\frac{dz}{dx}\right)^2\right] \tag{7.15}$$

By assuming $\theta << 1$, Eq. (7.15) can be rewritten simply as

$$dF_x = \left[C_N \frac{dz}{dt} - \overline{V}_x\left(C_N - C_L\right)\frac{dz}{dx}\right]dx \tag{7.16}$$

Now the force F_z, which is calculated by

$$F_z = \int_{x=0}^{x=l} dF_z \tag{7.17}$$

is not the moment of force but the propelling force directed to the z axis. To calculate the moment of force M, the distance $r(x)$ from the x position of δs and the center of mass of the IPMC should be multiplied by δF_z and integrated as

$$M = \int_{x=0}^{x=l} r(x) dF_z \tag{7.18}$$

7.12 Applying Propulsion Model

In the previous section, we presented the propulsion model of the swimming motion in which the position $z(x,t)$ of each point of the IPMC should be determined to calculate the propelling and turning forces of the robot. In this study, we extracted $z(x,t)$ from the real bending motion of the experiments and applied it to the propulsion model to calculate the propelling force.

Moreover, the drag resistance coefficient C_L and normal resistance coefficient C_N should be given in the model. However, we did not estimate them by ourselves and used only the values described in a previous study [9], in which the coefficients of drag resistance of a cylinder C_L = 0.82 and of normal resistance of a circular plate C_N = 1.17 were obtained. These values may not be so different from the true values, although precise measurements for real IPMC devices should be an important future work.

7.12.1 Extracting Bending Motion

To extract the position $z(x,t)$ of each point of the IPMC, we captured a sequence of images of the bending motion in our experiments and extracted the bending curve, as shown in Figure 7.39. We sampled 15 points with equal spaces on the extracted curved line, as shown in Figure 7.39(d).

These sets of points extracted from the image sequence are the sampling points of $z(x,t)$ and were used to calculate the differential dz/dx and dz/dt in the propulsion model. Figure 7.40 shows an example of the extracted $z(x,t)$ and calculated differential dz/dx and dz/dt from the corresponding $z(x,t)$.

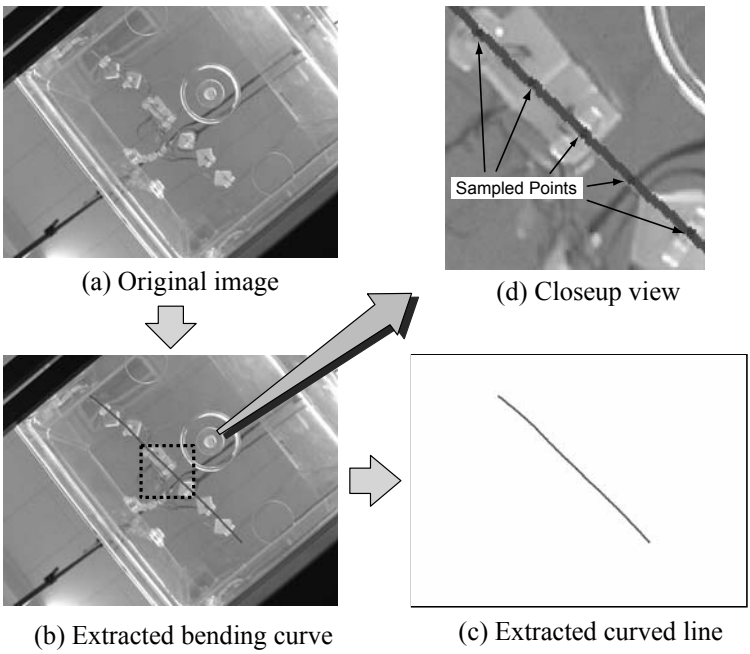

Figure 7.39. Extracted curved line from image

7.12.2 Applying Model on Forward and Backward Propulsions

We first calculated the propelling force F_x by (7.13) using $z(x,t)$ extracted from the experiments of forward and backward propulsions. This F_x varies with a change in average propelling speed $\overline{V}_x$, as shown in Figure 7.41.

Generally, when a robot is propelling at a constant speed, the propelling force F_x is zero. In this case, if $F_x = 0$ in the result of the analysis shown in Figure 41, the forward and backward constant speeds are $V_x = -5.3\times10^{-4}$m/s and $V_x = 9.8 \times 10^{-4}$m/s, respectively. On the other hand, the true forward and backward speeds measured in the previous experiment are $V_x = -4.2 \times 10^{-3}$m/s and $V_x = 3.5 \times 10^{-3}$m/s, respectively. These differences between the speeds of the real IPMC and the speeds analyzed from the model can be induced by the force that is not proportional to the speed and not considered in this model.

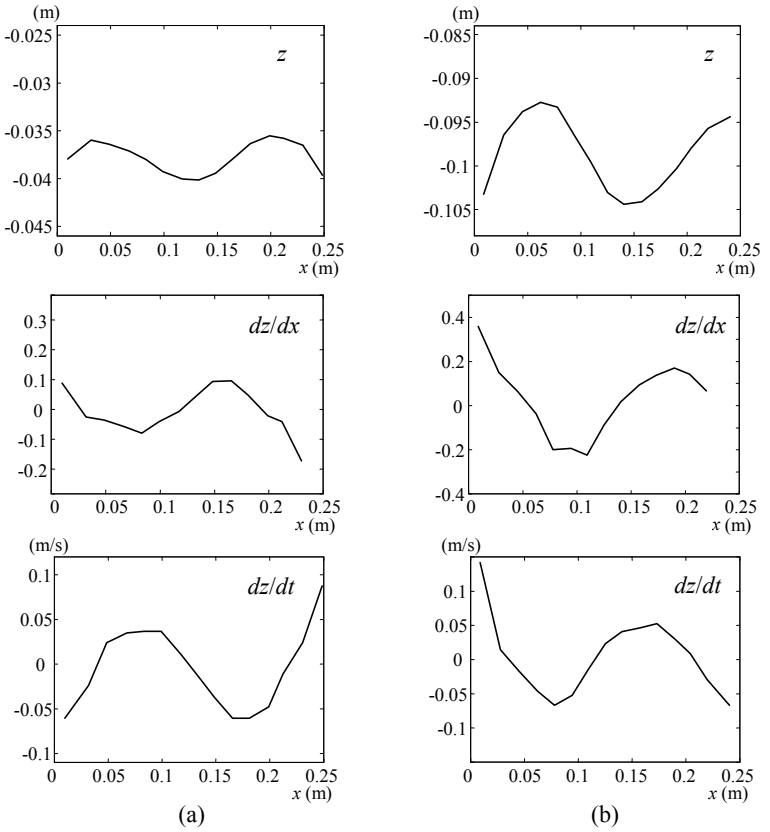

Figure 7.40. Examples of extracted plots of (a) forward and (b) backward propulsions

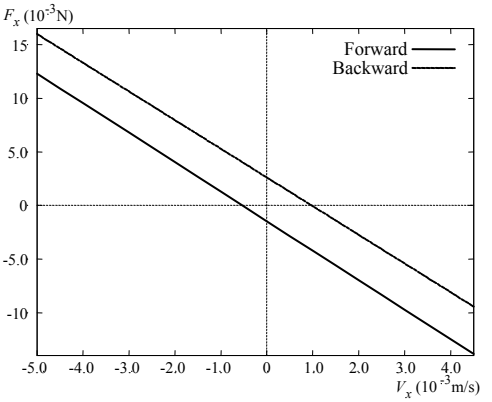

Figure 7.41. Propulsion force vs. propelling speed

7.12.3 Applying Model to Right Turn and Left Turn

We next calculated the moment of force M by (7.18) using $z(x,t)$ extracted from the experiments of the right turn and left turn of the IPMC. This M varies with a change in average propelling speed $\overline{V_x}$, as shown in Figure 7.42.

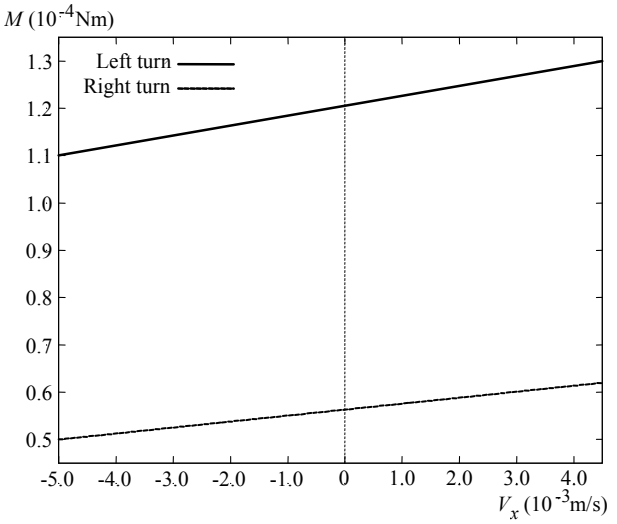

Figure 7.42. Moment of force vs. propelling speed

By fixing V_x as zero, the moments of force $M = 1.2 \times 10^{-4}$ Nm for the left turn and $M = 5.6 \times 10^{-5}$ Nm for the right turn are obtained from Figure 7.42. These values indicate the moments of force for the left turn on both. Although this is not true, comparing the relative differences between the two values obtained, the moment of force for the left turn is larger than that for the right turn, which is considered a reasonable result. These biased results can be induced by an error in the estimation of the moment center of the IPMC. In the analysis, we calculated only the average position of the 15 sampled points as the moment center, which may not be accurate. Moreover, force that is not proportional to speed can be the other reason for this error.

7.13 Conclusions

In this study, we described our new type of multi-DOF manipulator using a patterned artificial muscle (IPMC), and proposed the kinematic modeling of multi-link motions for the control of the manipulator using an inverse Jacobian or a transposed Jacobian with visual sensing. Simulations and experiments verify our approach. Our future work should address the problem of the low conductivity of segment interconnections. We can increase the width of the interconnections

and/or increase the amount of gold plating, so that their conductive layers become thicker. Another issue is the dynamic aspect of the bending motions of the IPMC membrane. Although bending velocity generally follows a given voltage signal, nonlinear characteristics, such as swing back motion, also contribute to a dynamic response. Extensive work has been carried out to identify and model the dynamics. In the future, we will examine these models and realize dynamic control of an IPMC manipulator.

We have also developed a biomimetic snake-like swimming robot using an IPMC. We demonstrated that the swimming speed and direction can be controlled using a patterned IPMC. The IPMC has segments, each of which can be controlled individually. By inputting sine waves with different phases, we can make progressive waves move along the body of the IPMC, and these waves induce an impelling force. We also proposed an analytical model for the robot propulsion considering the drag and resistance forces induced by the bending motion of the IPMC. We applied the results of the experiments to the proposed model and estimated the propelling forces of the robot propulsion. The following are our future plans: (1) make an IPMC that can generate a stronger impelling force and swim faster and (2) mount a battery and a controlling circuit on the IPMC, instead of connecting them to a host PC.

7.14 References

[1] K. Asaka and K. Oguro (2000) Bending of polyelectrolyte membrane platinum composites by electric stimuli Part II. Response kinetics. J. of Electroanalytical Chemistry, 480:186–198.

[2] Y. Bar-Cohen (2002) Electro-active polymers: current capabilities and challenges. Proc. of SPIE Int. Symp. on Smart Structures and Materials, EAPAD

[3] J. Gray (1957) The movement of the spermatozoa of the Bull. J. of Experimental Biology, 35(1):97–111.

[4] J. Gray and G. J. Hancock (1955) The propulsion of sea-urchin spermatozoa. J. of Experimental Biology, 32:802–814.

[5] S. Guo, T. Fukuda, and K. Asaka (2003) A New Type of Fish-Like Underwater Microrobot. IEEE/ASME Trans. on Mechatronics, 8(1):136–141.

[6] S. Guo, T. Fukuda, K. Kousuge, F. Arai, K. Oguro, and M. Negoro (1995) Micro catheter system with active guide wire. Proc. IEEE Int. Conf. on Robotics and Automation, 79–84.

[7] Y. Hiramoto (1979) Flagellar movements. J. of the Japan Society of Mechanical Engineers, 82(732):1003–1007. (in Japanese)

[8] M.J. Lighthill (1960) Note on the swimming of slender fish. J. Fluid Mechanics, 9:305–317.

[9] M. Makino (1991) Fluid resistance and streamline - design of vehicle shape from viewpoint of hydrodynamics -. Sangyo-tosho press. (in Japanese)

[10] K. Mallavarapu and D. J. Leo (2001) Feedback control of the bending response of ionic polymer actuators. J. of Intelligent Material Systems and Structures, 12:143–155.

[11] M. Mojarrad and M. Shahinpoor (1997) Biomimetic robotic propulsion using polymeric artificial muscles. Proc. IEEE Int. Conf. on Robotics and Automation, 2152–2157.

[12] Y. Nakabo, M. Ishikawa, H. Toyoda, and S. Mizuno (2000) 1 ms column parallel vision system and its application of high speed target tracking. Proc. IEEE Int. Conf. on Robotics and Automation, 650–655.
[13] Y. Nakabo, T. Mukai, and K. Asaka (2004) A multi-DOF robot manipulator with a patterned artificial muscle. The 2nd Conf. on Artificial Muscles. Osaka
[14] Y. Nakabo, T. Mukai, and K. Asaka (2005) Kinematic modeling and visual sensing of multi-DOF robot manipulator with patterned artificial muscle. Proc. IEEE Int. Conf. Robotics and Automation, 4326–4331.
[15] Y. Nakabo, T. Mukai, K. Ogawa, N. Ohnishi, and K. Asaka (2004) Biomimetic soft robot using artificial muscle. IEEE/RSJ Int. Conf. Intelligent Robots and Systems, in tutorial, WTP3 Electro-Active Polymer for Use in Robotics.
[16] K. Ogawa, Y. Nakabo, T. Mukai, K. Asaka, and N. Ohnishi (2004) A snake-like swimming artificial muscle. The 2nd Conf. on Artificial Muscles. Osaka
[17] K. Ogawa, Y. Nakabo, T. Mukai, K. Asaka, and N. Ohnishi (2005) Snakelike swimming artificial muscle. Video Proc. IEEE Int. Conf. Robotics and Automation.
[18] K. Oguro, Y. Kawami, and H. Takenaka (1992) Bending of an ion-conducting polymer film-electrode composite by an electric stimulus at low voltage. J. of Micromachine Society, 5:27–30. (in Japanese)
[19] S. Tadokoro, S. Yamagami, M. Ozawa, T. Kimura, and T. Takamori (1999) Multi-DOF device for soft micromanipulation consisting of soft gel actuator elements. Proc. of IEEE Int. Conf. on Robotics and Automation, 2177–2182.
[20] T.Y. Wu (1961) Swimming of waving plate. J. of Fluid Mechanics, 10:321–344.